Journal of Catalysis 393 (2021) 140–148

Contents lists available at ScienceDirect

Journal of Catalysis

journal homepage: www.elsevier.com/locate/jcat

1D metal-dithiolene wires as a new class of bi-functional oxygen reduction and evolution single-atom electrocatalysts

Qingming Deng [a,b,*], Jin Han [a], Jiong Zhao [c], Guibin Chen [a], Tejs Vegge [b], Heine Anton Hansen [b,*]

[a] *Physics Department and Jiangsu Key Laboratory for Chemistry of Low-Dimensional Materials, Huaiyin Normal University, Huaian 223300, China*
[b] *Department of Energy Conversion and Storage, Technical University of Denmark, Anker Engelunds Vej, Building 301, 2800 Kgs. Lyngby, Denmark*
[c] *Department of Applied Physics, The Hong Kong Polytechnic University, Kowloon, Hong Kong*

ARTICLE INFO

Article history:
Received 8 July 2020
Revised 10 November 2020
Accepted 11 November 2020
Available online 26 November 2020

Keywords:
Computational screening
Oxygen reduction reaction
Oxygen evolution reaction
Bifunctional ORR/OER Catalyst
Density functional theory
Single-atom catalysts

ABSTRACT

Discovering low-cost, durable and highly active electrocatalysts with reduced use of precious platinum group metals (PGM) as catalysts for the hydrogen evolution reaction (HER), the oxygen reduction reaction (ORR), and the oxygen evolution reaction (OER) is a key step for large-scale adaptation of fuel cells, electrolyzers, and metal-air batteries. Here we explore the stability and reaction mechanisms of synthesized one-dimensional transition metal dithiolene wire (TM-DWs, TM = Cr – Cu, Rh, Ir, Pt, Pd) for the ORR and the OER in acid solution by density functional theory (DFT) calculations. Our calculations reveal that Co-DW intrinsically exhibits high catalytic activity for bi-functional ORR/OER with low limiting overpotentials (η) of 0.46/0.45 V via four-electron reactions. These low limiting overpotentials arise from modified scaling relations by strengthening the binding free energy of OOH* compared to OH* on TM-DWs, yielding universal minimum ORR/OER overpotentials of η = 0.28/0.22 V, remarkably decreased compared to both metal and oxide surfaces (η_{ideal} = 0.37 V). By applying uni-axial strain, the adsorption strength of reaction intermediates on TM reactive sites can be optimized due to shifts in d-band centers. Our findings provide valuable insight into rational design of non-precious metals based electrocatalysts, and demonstrate a new strategy of tuning adsorptions via uni-axial strain to develop efficient bifunctional electrocatalysts of ORR/OER under optimal conditions.

1. Introduction

With rising concerns about limited fossil fuel resources, air pollution and climate changes, there are intense worldwide efforts to utilize more sustainable and renewable energy sources. Key technologies in the sustainable chain are electrochemical storage and conversion devices, such as metal-air batteries, water splitting systems, and proton exchange membrane (PEM) fuel cells (FC) [1,2]. As the key reaction in the PEMFC technology, the oxygen reduction reaction (ORR) occurs at the cathode with the production of water via the four-electron reduction. Platinum based materials are commonly used electrocatalysts for the ORR. However, the most important challenges are related to the much slower kinetics of the cathode than the anode reaction (hydrogen oxidation reaction) and the utilization of precious metals, which greatly hinder large-scale industrial applications [3]. Similarly, the hydrogen and oxygen evolution reaction (HER/OER) relevant to water splitting electrocatalysts also requires catalysts based on noble metals [4–6]. Thus, it is highly desirable to develop new classes of electrocatalysts based on earth-abundant materials, whose catalytic performances are comparable or even higher than those of noble metal-based materials [7]. Any technical breakthrough therefore would be greatly beneficial for easing the contradiction between supply and demand of energy and solving environmental problems. Great effort in recent years has been devoted by researchers working in this area, there are now a large number of such earth-abundant materials that are electrocatalytically active for either ORR or OER. For example, Liu et al. found that CoFe alloy embedded in N-doped carbon nanotubes presents appreciable ORR/OER activity when applied in a Zn–air battery [8]. A series of manganese oxides (MnO_x, Mn_2O_3, Mn_3O_4) have been widely investigated and shown OER activity in alkaline and neutral solutions [9–12]. Whereas, MnO_2 shows favourable ORR activities after inducing carbon nanotubes [13]. The enhanced activity can be attributed to the accelerated electron transfer process [14]. Serov et al.

---

* Corresponding authors at: Physics Department and Jiangsu Key Laboratory for Chemistry of Low-Dimensional Materials, Huaiyin Normal University, Huaian 223300, China (Q. Deng). Department of Energy Conversion and Storage, Technical University of Denmark, Fysikvej, 2800 Kgs. Lyngby, Denmark. (H. Hansen)

E-mail addresses: Qingmingdeng@gmail.com (Q. Deng), heih@dtu.dk (H. Anton Hansen).

https://doi.org/10.1016/j.jcat.2020.11.016
0021-9517/© 2020 The Author(s). Published by Elsevier Inc.

systematically studied the roles of influences of different preparation methods on electrocatalytic activity for ORR and OER of $CuCo_2O_4$ and found sacrificial support method prepared catalysts can serve as highly active bi-functional catalysts in both ORR and OER [15]. It has been shown that transition metal oxides (e.g., Mn, Co, Ni, and Fe etc.) display high intrinsic activity and stability in electrochemical reactions as bifunctional ORR/OER catalysts [16].

Single-atom catalysts (SACs), which refer to a class of catalysts with catalytically active isolated single metal atoms, have recently stimulated extensive efforts worldwide to develop low-cost, earth-abundant multi-functional electrocatalysts to promote the ORR, OER, and HER. A wide variety of single metal atoms can strongly and orderly anchor on support surfaces possessing great potential for achieving high-activity catalysts with maximal usage of the metals [17–19]. Besides, the simple structures provide important atomic insights into the fundamental understanding of the nature of the active sites and identify intrinsic reaction mechanisms of the catalysts. Low-dimensional metal–organic frameworks (MOFs) with intrinsic structural porosity, large surface-to-volume ratio, chemical tunability and high charge carrier mobility have been regarded as promising SACs for next-generation renewable-energy applications [20–22]. These materials are synthesized through a bottom-up approach, by combining aromatic organic moieties that can ligate square-planar metal ions. Up to now, the catalytic performances of the transition metal-N_4 macrocycles (TM-N_4), e.g. phthalocyanine (TM-Pc) [23–28], TM-porphyrin-like complexes (TM-PP) [29–31] and TM coordinated hexaaminobenzene-base polymer (TM-HAP) [32–33], and TM-tetracyanoquinodimethane (TM–TCNQ) [34–38] have been extensively studied both experimentally and theoretically.

Recently, a new class of MOFs, named transition metal dithiolenes wires (DW), have been synthesised in one- and two-dimensional frameworks by Marinescu et al. [39–40]. They found Co- and Ni-DWs are efficient electrocatalysts for the HER. The experimentally measured overpotential of Ni-DWs could be 470 mV at a current density of 10 mA cm^{-2} at pH 1.3, which is 90 mV lower than that of the Co-DW. Besides, no decrease in activity is observed for the Ni complex during the first hour of electrolysis, suggesting remarkable stability under very acidic aqueous solutions. Analogous to the structures of TM-N_4 complexes, TM atoms are embedded periodically into four-coordinated sulfur macrocycles with very high density (ca. 2.3×10^{21}/g) as shown in Fig. 1. Thus, the question naturally arises whether they can be used as good electrocatalysts for the ORR or the OER, and which TM-DWs exhibit the best performance. To the best of our knowledge, there are no previous theoretical nor experimental studies of this appealing issue. Therefore, we extensively explore a series of TM-DW (TM = Cr – Cu, Rh, Ir, Pt, Pd) as ORR and OER electrocatalysts by means of density functional theory (DFT) computations. Our results suggest that synthesised Co-DW intrinsically shows good catalytic activity for bi-functional ORR/OER with the low limiting overpotentials (η) of 0.46/0.45 V via the four-electron reaction. This significant improvement arises from modified scaling relation by strengthening binding free energy of OOH compared to OH on TM-DWs, yielding universal bifunctional minimum ORR/OER overpotentials of η = 0.28/0.22 V. By applying uni-axial strain, activities of Co-DW for ORR and OER can been further boosted, e.g. η = 0.31/0.47 V under 5% compressive strain due to varying d-band centers with optimal absorptions. Besides, Co-DW possesses superior electrical conductivity allowing fast electron transfer during the reaction. Hence, the Co-DW is a quite promising SAC for bi-functional ORR/OER.

2. Computational methods

Our studies are based on spin-polarized density function theory (DFT) calculations within the generalized gradient approximation (GGA) [41] as implemented in the Vienna ab initio simulation package (VASP) program package [42] to explore the reaction mechanisms for the ORR and the OER on TM-DWs. The exchange–correlation interactions are described with the BEEF-vdW [43] functional, which is specially designed to provide more accurate descriptions of van der Waals dispersive forces and chemisorption energies of molecules on surfaces than the PBE functional, and also provides the opportunity to establish uncertainties on the predicted energies. The kinetic energy cutoff for the plane-wave basis set is to 500 eV, and adsorption of OOH*, O*, and OH* is allowed on only one side of the exposed TM-DWs with dipole corrections in the Z direction. Solvation is considered through a self-consistent polarizable continuum model with a dielectric constant of 78.4 for water [44]. The thickness of the vacuum layer is set to be more than 20 Å, which is sufficiently large to avoid interlayer interactions. The electronic SCF tolerance is set to 10^{-5} eV. Fully relaxed geometries and lattice constant are obtained by optimizing all atomic positions until the Hellmann–Feynman forces are less than 0.02 eV/Å. The k-point samplings with a gamma-centred Monkhorst-Pack scheme [45] are $15 \times 1 \times 1$ in the Brillouin zone for structure optimizations, while a $25 \times 1 \times 1$ mesh is used for the density of states (DOS) calculations. Free energy corrections are calculated by the quantum mechanical harmonic approximation and ideal gas approximation in the Atomistic Simulation Environment (ASE) [46].

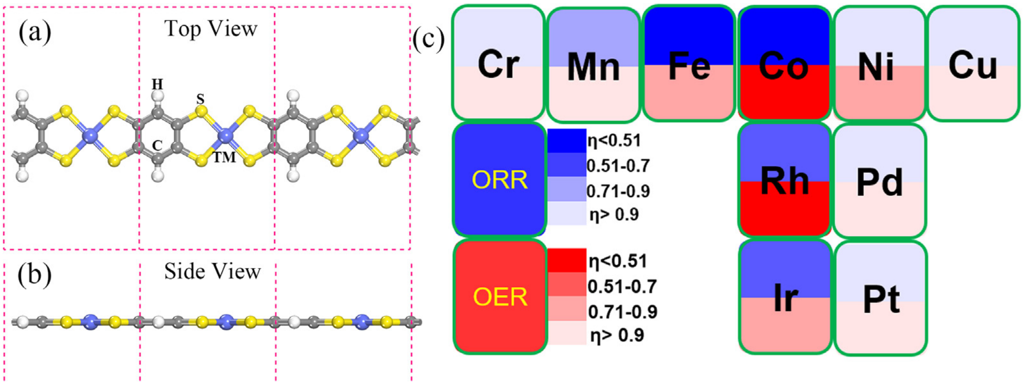

Fig. 1. Top (a) and side (b) views of ten TM-DWs (TM = Cr-Cu, Rh, Pd, Ir, Pt) candidates. (c) Bluer and redder colours correspond to lower limiting overpotentials (η) toward ORR and OER, respectively. Blue, transition metals (TM); yellow, sulfur (S); gray, carbon (C), and white, hydrogen (H).

The DFT adsorption energies of OOH*, O*, and OH* are calculated with reference to H_2O and H_2 according to the following Eqs. (1)–(3):

$$\Delta E_{ads}(OOH^*) = E_{DWs-OOH} - E_{DWs} - (2E_{H2O} - 3/2E_{H2}) \tag{1}$$

$$\Delta E_{ads}(O^*) = E_{DWs-O} - E_{DWs} - (E_{H2O} - E_{H2}) \tag{2}$$

$$\Delta E_{ads}(OH^*) = E_{DWs-OH} - E_{DWs} - (E_{H2O} - 1/2E_{H2}) \tag{3}$$

where $E_{DWs\text{-}OOH}$, $E_{DWs\text{-}O}$, $E_{DWs\text{-}OH}$ are the energies of adsorbates binding on transition metal dithiolene wires, E_{H2O} and E_{H2} is the total energy of single isolated H_2O and H_2 molecules, respectively.

The Gibbs free energy change of adsorbates in acid is evaluated by the equation

$$\Delta G = \Delta E_{ads} + \Delta E_{ZPE} - T\Delta S + \Delta\int C_p dT + \Delta G_U + \Delta G_{pH} \tag{4}$$

where ΔE_{ads} is DFT adsorption as shown as in Eqs. (1)–(3). ΔE_{ZPE}, $T\Delta S$ and $\Delta\int C_p dT$ are related to the zero point energy change, entropy change, and the heat capacity change upon adsorption. Free energy corrections in standard states (298 K, 1 bar) of adsorbates (sum of ΔE_{ZPE}, $T\Delta S$ and $\Delta\int C_p dT$) are approximated by the constant values of 0.4 eV, 0.05 eV and 0.35 eV for OOH, O, and OH adsorbates obtained for Co-DW, respectively. The effect of the electrode potential on the chemical potential of an electron can be expressed as $\Delta G_U = -neU$, where n is the number of transferred proton-electron pairs and U is the electrode potential versus the standard hydrogen electrode [30]. $\Delta G_{pH} = 2.303k_BTpH$ is the free energy correction based on the H^+ concentration, where k_B and T are the Boltzmann constant and temperature, respectively. We consider pH = 0 for the acid medium in our study. As rather small barriers are found for proton coupled electron transfer [47], we assume the reaction kinetics is determined by the free energy change of each step. The optimized structures of TM-DWs are planar without bulking. Thus, similar to other flat structural materials, pre-adsorbated O_2 is difficult to dissociate into two O*, which is usually related to a high energy barrier of dissociation of O_2 on single metal atom sites due to the limited space to accommodate two atomic O*.[48] Therefore, a direct four-electron pathway becomes prohibitive via a dissociative mechanism, and we only consider the associative mechanism in current study.

3. Results and discussion

3.1. The oxygen reduction reaction and oxygen evolution reaction catalyzed by TM-DWs

Three key adsorption intermediates determine the final catalytic performance towards the ORR and the OER. If a catalyst binds one or more intermediates too strongly, the active sites are being occupied and poisoned; whereas if the interactions are too weak, reactants or intermediates are able to detach from the catalysts without reacting. Via the four-electron reaction pathway, the overall reaction free energy of the OER is 4.92 eV and in order to minimize free energy barriers, the adsorption free energies of consecutive intermediates OH*, O*, and OOH* are ideally separated by 1.23 eV, resulting in ideal adsorption free energies of OOH*, O*, and OH* of 3.69, 2.46, and 1.23 eV, respectively. The closer individual adsorption energies are to the ideal values, the higher catalytic activities can likely be achieved. To evaluate the activities of the TM-DWs, we first compute adsorption free energies of reaction intermediates (based on Equation (4)) on TM-DWs in Fig. 2 and table S2 in supporting information. The trend in binding strength is followed as Cr > Mn > Fe > Ir > Co > Rh > Ni > Pt > Pd > Cu. It is well known that occupied d-orbitals with lower energy level normally correlate with weaker interaction between the catalysts and reaction intermediates. We can see that the order of adsorption energies match with trend of d-band centers with the increase of the atomic number of TM atoms within each row. Among them, intermediate free energies on Co– and Ir-DWs are the closest to the ideal values with expecting high catalytic activities towards the ORR and the OER. Fig. 2 shows correlations between the binding free energies of ΔG(OH*) vs ΔG(O*) and ΔG(OH*) vs ΔG(OOH*) on a variety of TM-DWs. They can be expressed as linear functions of ΔG(OH*) by

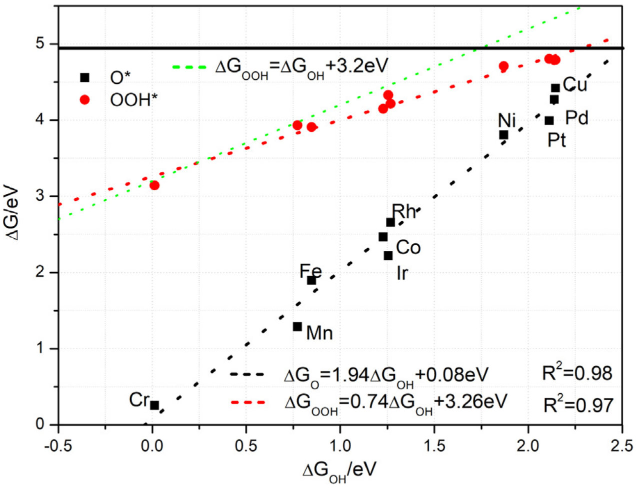

Fig. 2. Scaling relations between the adsorption free energies of adsorbates on TM-DWs. Black: O* vs. OH*; red: OOH* vs. OH*. The black line is at 4.92 eV, which is equal to formation energy by two water. The green dash line is a traditional scaling relation between OH* and OOH* for comparison.

$$\Delta G(O^*) = 1.94\Delta G(OH^*) + 0.08\ \text{eV} \tag{5}$$

$$\Delta G(OOH^*) = 0.74\Delta G(OH^*) + 3.26\ \text{eV} \tag{6}$$

Linear relations with high coefficients of determination ($R^2 = 0.92, 0.98$) are found. As the bond-order of O* vs. OH* should be 2 vs. 1, the expected slope of ~ 2 is very close to the fitted value of 1.94 in equation (5), and in agreement with previous predictions [49]. Similarly, the expected slope for OOH* vs. OH* should be ~ 1, as found on metal and oxide surfaces [50–51] based on electron-counting rules. On metals and oxides, the scaling relation between OH∗, and OOH ∗ species, implies universally minimal ideal overpotentials of ~0.37 V for the ORR and the OER [52], which impose a significant limitation to discovery of highly active electrocatalysts. Whereas for SCAs based on low dimensional materials, the slope between OH* and OOH* is usually smaller (ca.0.7 ~ 0.9) [32,49,53] than that on metals and oxides (~1.0), thereby allowing new possibilities for catalyst design compared to e.g. metals or oxides. The observed slope for OH vs OOH on TM-DWs is 0.74 with strengthened interactions of OOH* compared to OH* as shown as in Fig. 2. The reduced slope is mainly attributed to highly covalent metal–oxygen bonds, in which there is little charge transfer between active site and adsorbates as proposed by Calle-Vallejo et al.[53] Thus, we calculate the Bader charge of three intermediates on various TM-DWs. We note that the charges on different metals change little for O* and OH*. The charges on H atoms in OH* (~0.61–0.69|e|) and OOH* (~0.65–0.72|e|) remain approximately constant regardless of the type of metal. Besides, mean charges on O in O* and OH* are −0.54 |e| and −1.02 |e| with small deviations of 0.049 |e| and 0.056 |e|, respectively. However, the excess charges of OOH* decline rapidly from Ni to Pd as significant change of O—O moiety with a large deviation of 0.126 |e|. Besides, the O—O moiety charge increases for Ni, Cu, Pd and Pt (less negative), then the O—O atoms become less electron rich in figure S1, which means that the M—O should be less polarized. In Fig. S2, local DOS analysis reveals that the 2p orbitals of O atom bound to the TM in OOH* for Ni, Cu, Pd and Pt are narrow and near the fermi level, similar to O_2 molecularly adsorbated on metals [54]. Whereas, from Cr to Co, 2 π^* orbitals are diffuse in deeper energy regions and show stronger hybridizations with 3d-orbtials, indicating strong interaction between metal and OOH*. The 2p-band of O shifts to higher energies is indicative of a higher O basicity from Cr to Pt, suggesting the covalency of the TM—O bond decreases. It should, however, be noted that the slope of OOH* vs. OH* increases from 0.74 to 0.87 after excluding weakly binding Ni, Cu, Pd and Pt, which makes the slope approach the expected value of 1 from electron-counting rules.

We consider the following four electron ORR mechanism in acidic solution via Eqs. (7)–(10):

$$^* + O_2\ (g)\ +\ H^+ + e^- \rightarrow OOH^* \tag{7}$$

$$OOH^* + H^+ + e^- \rightarrow O^* + H_2O \tag{8}$$

$$O^* + H^+ + e^- \rightarrow OH^* \tag{9}$$

$$OH^* + H^+ + e^- \rightarrow {}^* + H_2O \tag{10}$$

From Eqs. (7)–(10), the reaction Gibbs free energy at 0 V vs RHE can be written as

$$\Delta G_1 = \Delta G\ (OOH^*) - 4.92\ \ eV \tag{11}$$

$$\Delta G_2 = \Delta G\ (O^*) - \Delta G\ (OOH^*) \tag{12}$$

$$\Delta G_3 = \Delta G\ (OH^*) - \Delta G\ (O^*) \tag{13}$$

$$\Delta G_4 = -\ \Delta G\ (OH^*) \tag{14}$$

The Gibbs free energy of O_2 is set as 4.92 eV from the formation free energy of two water molecules: $2H_2O \rightarrow O_2 + 2H_2$. We calculate $\Delta G_{1\text{-}4}$ using the computational hydrogen electrode (CHE) [55] to approximate the free energy of a proton and an electron by half the free energy a hydrogen molecule at U = 0 V vs RHE. The first step of the ORR pathway is O_2 being hydrogenated to OOH* at the active site. Then OOH* is hydrogenated to atomic oxygen and a free water molecule. Then, the adsorbated O* is attacked by an additional proton-electron pair to form OH*, which can be further reduced to the second H_2O. Here, the catalytic performance for ORR can be estimated by the thermodynamic limiting potential (U_{lim}) from equation (15).

$$U_{lim} = -\ \max\Delta G_1,\ \Delta G_2,\ \Delta G_3,\ \Delta G_4/e \tag{15}$$

The theoretical limiting overpotential (η), which depends on U_{lim} at standard conditions (pH = 0 and T = 298.15 K) is obtained from equation (16) by determining the magnitude of the potential-determining step at the equilibrium potential of 1.23 V

$$\eta^{ORR} = 1.23 - U_{lim} = 1.23 + \max\Delta G_1,\ \Delta G_2,\ \Delta G_3,\ \Delta G_4/e \tag{16}$$

Here, lower η represents a higher ORR activity. According to Eqs. (5)–(6) and (16), the theoretical overpotential can be further expressed as a function of the two variables ΔG(O*–OH*) and ΔG(OH*). Plotting volcano contour map of η^{ORR} for the class of TM-DWs in Fig. 3, leads to a universal minimum η^{ORR} of 0.28 V. The best catalysts for the ORR are found to be Fe- and Co-DWs with η^{ORR} of 0.38 and 0.46 V with different potential-determining steps. Compared to Pt(111), the values of ΔG(OOH*) are close, but absorption of O* and OH* is stronger on Pt(111) yielding a higher η^{ORR} of 0.65 V with the BEEF-vdW functional calculation [56] (Table S2 in Supporting Information). Rh-, Ir-DWs also exhibit good activity for the ORR with the potential-determining step being the reduction O_2 to OOH*. Too strong binding on Cr- and Mn-DW or too weak binding on Ni-, Cu-, Pd-, and Pt-DW result in high η^{ORR} on these metal sites.

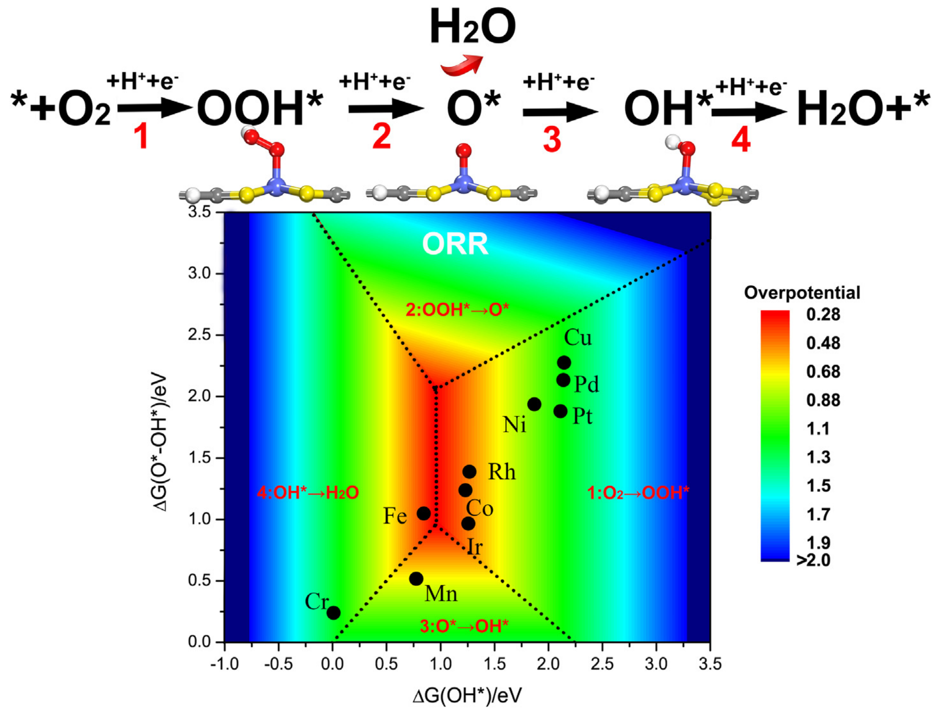

Fig. 3. Four-electron ORR pathway *via* the associative mechanism with the three intermediates OOH*, O* and OH*, and coloured contour of the limiting overpotential (η^{ORR}) as a function of the Gibbs free energies of O*–OH* and OH*. Oxygen (O) and hydrogen atoms are coloured in red and white. The volcano plot is based on Eqs. (5), (6) and (16).

We also study the two-electron ($2e^-$) reduction of O_2 to H_2O_2 through the formation of OOH^* followed by

$$OOH^* + H^+ + e^- \rightarrow ^* + H_2O_2 \tag{17}$$

Fig. 4 displays the free energy diagram for the ORR via the two-electron and four-electron reductions on Co-DW at different electrode potentials, respectively. At U = 0, the reactions from O_2 to H_2O or H_2O_2 can spontaneously happen on a Co-DW as an exothermic process. However, the formation of H_2O_2 via the two-electron pathway is less efficient compared to the production of O* in the $4e^-$ reduction, because the released free energy (0.65 eV) by H_2O_2 formation is much less than the free energy (1.68 eV) released from OOH* to O* and H_2O, which is consistent with previous results [49]. When $U = U_{lim} = 0.77$ V, the free energy of O_2 to OOH* is isoenergetic. A thermodynamic barrier of 0.46 eV is present for the potential-determining step at the equilibrium potential of 1.23 V, which is the reduction of O_2 to OOH* for the $4e^-$ reduction.

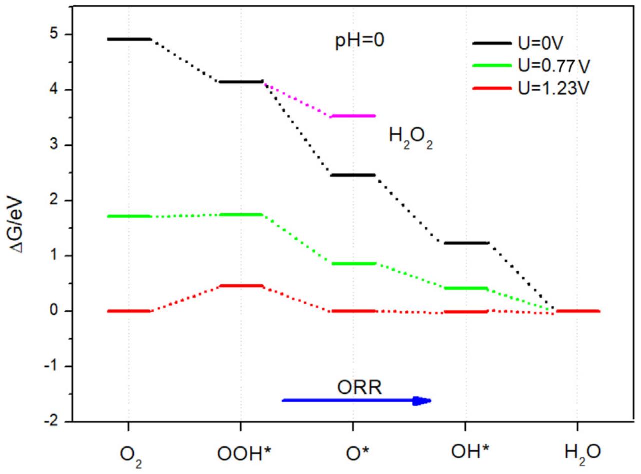

Fig. 4. Gibbs free energy landscape for the ORR on Co-DW at different electrode potentials in an acidic medium.

The oxygen evolution reaction is a key step in water splitting and metal-air battery technologies. Thus, we next explore the OER performance for TM-DWs. As the reverse reaction of the ORR, the limiting overpotential of the OER can be obtained via the following equation

$$\eta^{OER} = U_{lim} - 1.23\ V = \max{-\Delta G_1, -\Delta G_2, -\Delta G_3, -\Delta G_4}/e - 1.23\ V \tag{18}$$

As shown in Fig. 5, the ideal minimum η_{lim} is 0.22 V, which is much lower than that of metal or oxide surfaces as previously mentioned. Rh- and Co-DWs (η^{OER} = 0.33 and 0.45 V) locate at near the top of the OER volcano with the highest activities among the 10 candidates, which are comparable value to widely commercial use of RuO_2 [50] (η^{OER} = 0.42 eV). Fe-DW exhibits moderate activity with η^{OER} of 0.78 V. Potential-determining steps for the four-electron evolution on TM-DWs are distributed into three different zones. The best catalysts, Rh- and Co-DWs, have OOH* formation from O* as the potential-limiting step. A wide potential window has been considered, since at large potentials the active site could be covered by O or OH ligands. Therefore, we further analyse of the influence of adsorbates on the oxidized Co-DW for OER activity. When electrode potential reaches at 1.23 V, adsorption energies of O* and OH intermediate become isoenergetic in Fig. 4. And O* adsorption is more energetically preferred compared to OH* when potential is over 1.23 V for OER. The presence of O* on the back of Co-DW can weaken OOH*, O* and OH* by 0.6, 1.25 and 0.81 eV in Table S2, respectively. This makes OH oxidation to O as the potential limiting step with an overpotential of 0.8 V according to equation (18). A higher limiting potential of 2.03 V can be obtained, at which OER would proceed on both sides simultaneously. We notice

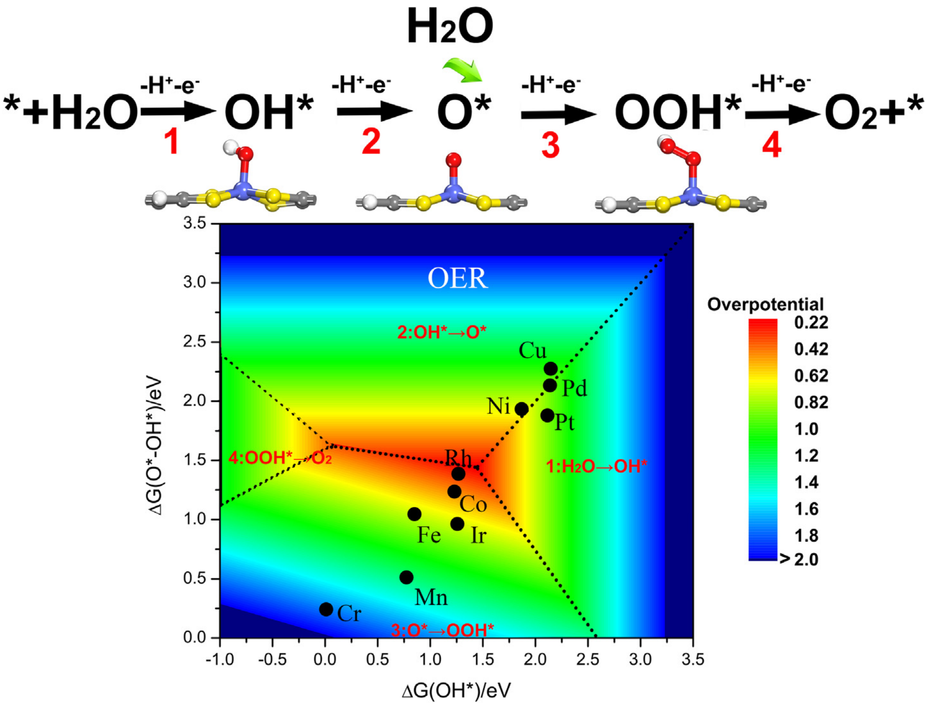

Fig. 5. Four-electron-transfer OER pathway via the associative mechanism with the three adsorbed intermediates of OOH*, O*, and OH*. A coloured contour of overpotential (η^{OER}) as a function of Gibbs free energies of O*–OH* and OH*. The volcano plot is based on Eqs. (5), (6) and (18).

that there is still space to reach the ideal minimum value for improving active of Co-DW by e.g. destabilizing the OH* intermediate. Considering the cost and limited abundance, we will not study noble metal-based catalysts further in the following.

3.2. Improving the catalytic performance by uni-axial strain

As we previously discussed, the catalytic activity is related to the metal d-band centers and their interaction with intermediates. Therefore, rational design of ideal SCAs with tunable d-orbital configuration for a certain electrocatalytic reaction may become a reality. In practice, applying strain on one-dimensional materials is expected as an effective technology to adjust electronic properties [57–60], which cannot be practically realized for 2D and 3D materials. For instance, Kaniber et al. use a piezoelectric device that loads carbon nanotubes (CNTs) on two Au pads as source and drain [61]. By applying different voltages, the electronic properties associated with axial length of CNT can be tuned. The adjustment of electronic properties induced by strain also affect the absorption of adsorbates [62] due to d-band center shifts [26]. We have recently shown that the ORR activity of Ni-TCNQ complexes can increase under 2–3% biaxial tensile strain. However, the catalytic performances of Fe-TCNQ for ORR/OER under strain are not improved [49]. DFT calculations confirm that the d-band centers of the strained Ni-TCNQ complexes increase linearly with strain. Distortion of the coordinated metals with four nitrogen atoms under strong strain may lead to vary free energy changes of ΔG (O*), ΔG(OH*) and ΔG(OOH*) to different degrees, which may provide more space to rational design novel SACs. Motivated by the above technology, we perform extensive calculations of TM-DWs (TM = Fe, Co) to study the impact of uni-axial strain on the catalytic performance. The strain, defined as $\varepsilon = (c_s - c_0)/c_0$ corresponds to tensile force (0 to +5%) and compressive force (-5% to 0), where c_s and c_0 is the lattice constant of the strained and the pristine TM-DWs, respectively. The potential-determining steps for the ORR or the OER don't change under strain. As clearly seen from the plots of limiting overpotential as a function of strain, η^{ORR} on Co-DW declines from 0.46 to 0.31 V, and η^{OER} corresponds to a higher value of 0.47 V corresponding to the best ORR/OER catalytic performance under 5% compressive strain, as shown in Fig.S3. While, low overpotential of 0.39 and 0.41 V for ORR/OER can also be obtained under 5% tensile strain. To gain a deeper insight into the effect of uni-axial stain, the variation of d-band centers and binding free energy are addressed. It can be seen that the values of d-band centers increase linearly with strain from ε −5% to + 5% with a slope of 0.0144 in Fig. 6 (a). The resulting binding interactions are, however, not linearly related to the d-band centers. When the tensile strain reaches + 5%, ΔG(OOH*) declines from 4.15 to 4.08 eV, and ΔG(O*) change slightly from 2.47 to 2.44 eV in Fig. 6. Thus, lower ΔG(OOH*) results in a lower η^{ORR} as the potential-determining step for the ORR is hydrogenation of O_2. Limiting overpotentials for the OER are determined by the energetic difference of ΔG(OOH*) and ΔG(O*) because the potential-determining step is OOH* formation from O*. Since OOH* is stabilized more than O* by 5% strain, η^{OER} decreases at 5% strain. Interestingly, Fe-DW exhibits a different trend in the d-band center and binding free energy. Here, ΔG increases linearly with strain while the d-band center follows a second-order polynomial as function of strain in Fig. 6 (c). The limiting overpotentials of Fe-DW for the ORR or OER decrease to minimal values under the tensile strain

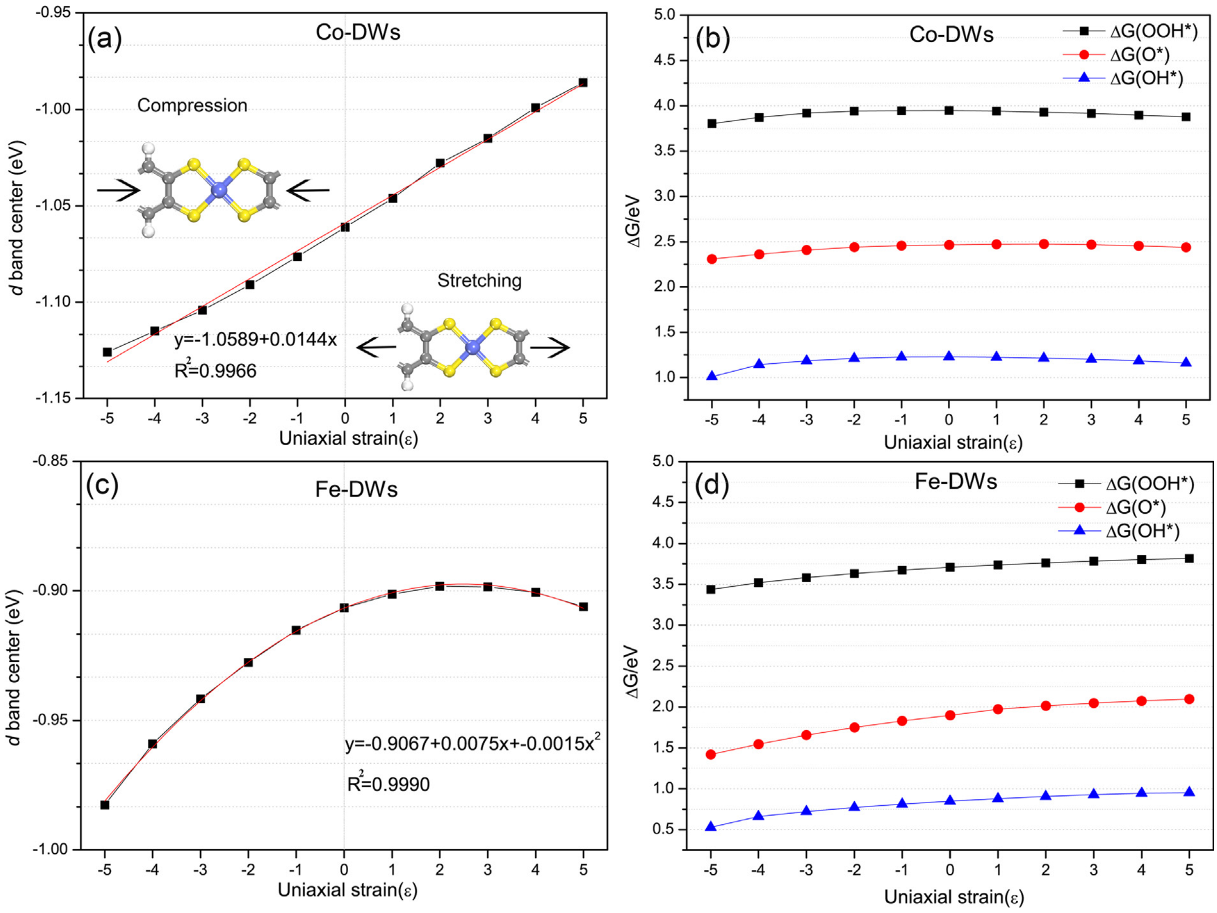

Fig. 6. The changes of *d*-band centers and Δ*G* on TM-DWs (TM = Co, Fe) under uni-axial stain.

of 5%. It could be relevant to strain that while 5% tensile and compressive stress can be very difficult to achieve for 3D and 2D materials, but the 1D character makes this possible here. We notice that the variations in binding free energies caused by strain are small. To realize a large space to optimize ΔG for the relative inactive candidates, grafting axial ligands on the TM sites as five coordination complexes can be taken into account [49,63]. As the ORR and OER catalytic activity of Co-DW almost reach the optimal values, we will not study the effect of axial ligands here. In brief, strain yields either linear or second order shifts of the d-band centers on Co– or Fe-DWs. The resulting catalytic activity of Co–, and Fe-DWs towards ORR/OER can be further boosted by artificially tuning d-band centers under uni-axial strain.

3.3. Solvation effects on Co-DW

Solvation is a crucial ingredient to predict accurate catalytic activities [64–69]. Solvation corrections obtained by either implicit or more computationally expensive explicit approaches can be very different [70,71], which may result in entirely different predictions of the overpotential and the rate-limiting step. The implicit approach has a minimal computational cost, and the parameters are normally fit to data on solvated molecules. By using implicit model, the week solvation effect with small deviation on various metals can be found in Table S2. The solvation energies of OOH*, O* and OH* on Co-DW are −0.22, −0.09 and −0.15 eV, which are agreed with the result (OOH*=−0.1 eV, OH*=−0.2 eV) by explicit model on Rh embedded N-doped double vacancies graphene as 2D-single-atom catalysis [72]. Thus, using both explicit or implicit solvation corrections yield consistent results for the system investigated here. It is worth noting that solvation energy is stronger and depend on the metal center for both metal surfaces [73] and molecular complexes [53]. For instance, explicit correction of OOH* and OH* are −0.25 and −0.5 eV using a static water bilayer to mimic the actual water structure near the solid/liquid interface on Pt(111)[55]. Solvation energies of OH* on the Cu (111), Au(111) and Pt(111) are −0.32, −0.68 and −0.58 eV, respectively [73].

3.4. Properties of 1D Co-DW

As SACs, single Co atoms are orderly distributed between four sulfur atoms forming a square macrocycle as shown in Fig. 1 and Fig. 7(a). In agreement with previously reported theoretical values [19,74], the Co-Co distance, corresponding to the lattice constant along the × axis, is 8.463 Å, which provides enough distance for the catalytic reactions and maximize the use of the metal atoms. The energy of the antiferromagnetic (AFM) state is slightly lower than that of the ferromagnetic (FM) state by 12 meV. Thus, we have simply used ferromagnetic unit cells as models to investigate the whole catalytic reaction processes. The spin density mainly accumulates on the Co atom (1.06μB), while the S atoms are nonmagnetic with slight magnetic moments of 0.01 μB as shown in Fig. 7(a). The four equivalent bond lengths between Co-S are 2.157 Å (Table S1 in Supporting Information), which are longer than the counterpart of cobalt coordinating in a PP sheet (1.931 Å). The inspection of electron localization function (ELF) as shown as in Fig. 7(b) demonstrates that the strong covalency of dithiolene ligands because of the high electron density. Few electrons are distributed around the Co atom because the coordinated S atoms (2.58) are more electronegative than the Co atom (1.88). Each sulfur atom of Co-DW only carries − 0.11 |e|, which is much less negative than that of nitrogen −1.15 |e| in Co-PP, and the neighbouring Co carries 0.66 |e| (1.11 |e| in Co-PP) positive charge based on Bader charge analysis respectively, which can be attributed to the weaker electronegativity of sulfur (2.58) than nitrogen (3.04). To get a deeper insight, we plot the spin-polarized local density of states (LDOS) for Co-3d and S-3p orbitals of Co-DW as shown as in Fig. S4. A strong hybridization between Co-3d and S-3p orbitals can be seen below the Fermi level (E_f) from strong Co-S coordination bonds. Wang et al. [19] proposed that Co-DW exhibits superior electrical conductivity with small effective masses of charge carriers. Its high electron/hole mobility is comparable to $CH_3NH_3PbI_3$ utilized organic–inorganic perovskite in solar cells [75]. It is evident that high electrical conductivity of Co-DW is an additional beneficial feature to allow fast electron transfer during the electrocatalytic processes.

To maintain catalytic durability for long-term use, strong binding of the central transition metals with the frame is essential to avoid metal detaching from the catalyst. Too weak binding strengths indicate the metal atoms are able to aggregate to form metal clusters, which usually happens on defect grapheme [76]. Therefore, we calculate the energetic difference (E_{diff}) between the cohesive energy of the bulk metal phase and the metal embedding energy of the TM-DWs to evaluate binding strength of metals into the 4S macrocyclic moiety (equations and values can be obtained in Table S1, Supporting Information). If $E_{diff} < 0$, we assume that incorporation of metals into the 4S macrocyclic moiety is preferred over forming metal clusters. Mn-DW can be first excluded. This is because the embedding energy of Mn with high or low spin states is higher than its cohesive energy by 1.21 eV. The stability against formation of metal clusters is Ni > Cu > Cr > Rh > Co > Ir > Fe > Mn. After applying this stability criteria, we conclude that Co can firmly anchor into the sulfur macrocyclic frames in acid condition during the electrochemical reaction.

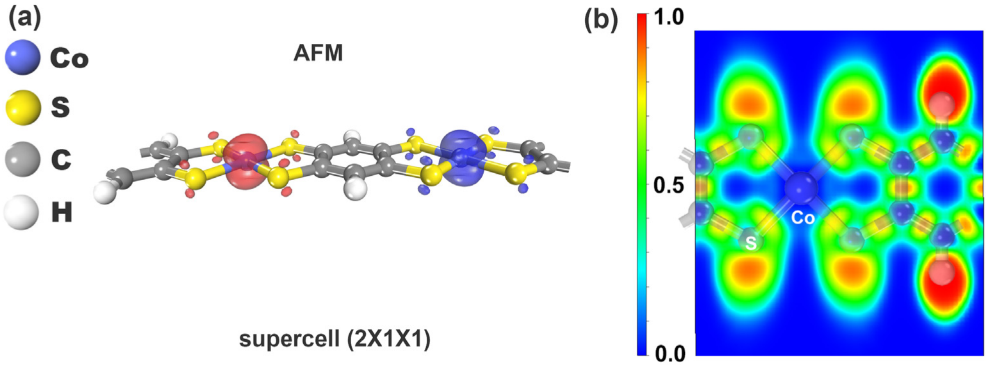

Fig. 7. (a) Spin-polarized density labeled on optimized supercell structure of Co-DW in AFM state. Spin up and spin down states are represented in blue and red. (b) The ELF of Co-SP ranges from 0 to 1 provides a better analysis of the chemical bonds. A value of the ELF close to one corresponds to a region of the space where there is a high probability of finding electron localization, whereas an ELF value close to one-half corresponds to a region of electron gas-like behavior.

4. Conclusion

To summarize, we have systematically investigated stabilities and catalytic behaviours of 10 TM-DWs toward the ORR and the OER by using density functional theory. The calculations reveal that Co-DW intrinsically exhibits high catalytic activities for bifunctional ORR/OER with the lower limiting overpotentials (η) of 0.46/0.45 V for the four-electron reaction by application of implicit solvation model. This significant improvement arises from modified scaling relations by strengthening the binding free energy of OOH* compared to OH* on TM-DWs, yielding minimum possible ORR/OER overpotentials of 0.28/0.22 V. Volcano plots of overpotentials as a function of $\Delta G(OH^*)$ and $\Delta G(O^*) - \Delta G(OH^*)$ indicate that O_2 hydrogenation to OOH* and the reaction of O* to OOH* are the potential-determining steps in the ORR and the OER on Co-DW, respectively. By applying uni-axial strain, the adsorption strength of reaction intermediates on TM active sites can be optimized due to tunable d-band centers. Consequently, the resulting activities of Co-DW for the ORR and the OER can be further improved under strain. Moreover, Co-DW possesses superior electrical conductivity allowing fast electron transfer during the reaction. As Co-DW is already experimentally synthesized, our findings provide important insight into the roles of the interaction between metal-sulfur macrocyclic frames and intermediates that go beyond the scope of precious metal based electrocatalysts, and demonstrate a new strategy of using the flexibility of the 1D-frame to tune the adsorption energies via application of uni-axial strain to achieve better catalytic performance.

Declaration of Competing Interest

The authors declare that they have no known competing financial interests or personal relationships that could have appeared to influence the work reported in this paper.

Acknowledgements

This work is supported by the National Natural Science Foundation of China (21703076, 51922113), the Natural Science Foundation of Jiangsu Province of China (BK20170466), Natural Science Research Program of Jiangsu Higher Education Institutions of China (18KJA140001), HK PolyU Project (1-ZE8C), and the Velux Foundations through the research center V-Sustain (grant 9455),Danmark.

Appendix A. Supplementary material

Supplementary data to this article can be found online at https://doi.org/10.1016/j.jcat.2020.11.016.

References

[1] T.V. Nguyen, R.E. White, A water and heat management model for Proton-Exchange-Membrane fuel cells, J. Electrochem. Soc. 140 (8) (1993) 2178–2186.
[2] H. Liu, B.E. Logan, Electricity generation using an air-cathode single chamber microbial fuel cell in the presence and absence of a proton exchange membrane, Environ. Sci. Technol. 38 (14) (2004) 4040–4046.
[3] C. Sealy, The problem with platinum, Mater. Today 11 (12) (2008) 65–68.
[4] T. Reier, M. Oezaslan, P. Strasser, Electrocatalytic oxygen evolution reaction (OER) on Ru, Ir, and Pt catalysts: a comparative study of nanoparticles and bulk materials, ACS Catal. 2 (8) (2012) 1765–1772.
[5] N.-T. Suen, S.-F. Hung, Q. Quan, N. Zhang, Y.-J. Xu, H.M. Chen, Electrocatalysis for the oxygen evolution reaction: recent development and future perspectives, Chem. Soc. Rev. 46 (2) (2017) 337–365.
[6] K.A. Stoerzinger, O. Diaz-Morales, M. Kolb, R.R. Rao, R. Frydendal, L. Qiao, X.R. Wang, N.B. Halck, J. Rossmeisl, H.A. Hansen, Orientation-Dependent Oxygen Evolution on RuO2 without Lattice Exchange, ACS Energy Lett. 2 (4) (2017) 876–881.
[7] R.R. Rao, M.J. Kolb, L. Giordano, A.F. Pedersen, Y. Katayama, J. Hwang, A. Mehta, H. You, J.R. Lunger, H. Zhou, Operando identification of site-dependent water oxidation activity on ruthenium dioxide single-crystal surfaces, Nat. Catal. (2020) 1–10.
[8] X. Liu, L. Wang, P. Yu, C. Tian, F. Sun, J. Ma, W. Li, H. Fu, A Stable Bifunctional Catalyst for Rechargeable Zinc-Air Batteries: Iron-Cobalt Nanoparticles Embedded in a Nitrogen-Doped 3D Carbon Matrix, Angew. Chem. Int. Ed. 57 (49) (2018) 16166–16170.
[9] A. Rafique, A. Massa, M. Fontana, S. Bianco, A. Chiodoni, C.F. Pirri, S. Hernández, A. Lamberti, Highly uniform anodically deposited film of MnO2 nanoflakes on carbon fibers for flexible and wearable fiber-shaped supercapacitors, ACS Appl. Mater. Interf. 9 (34) (2017) 28386–28393.
[10] Y. Gorlin, T.F. Jaramillo, A bifunctional nonprecious metal catalyst for oxygen reduction and water oxidation, J. Am. Chem. Soc. 132 (39) (2010) 13612–13614.
[11] H.-Y. Su, Y. Gorlin, I.C. Man, F. Calle-Vallejo, J.K. Nørskov, T.F. Jaramillo, J. Rossmeisl, Identifying active surface phases for metal oxide electrocatalysts: a study of manganese oxide bi-functional catalysts for oxygen reduction and water oxidation catalysis, PCCP 14 (40) (2012) 14010–14022.
[12] V. Tripkovic, H.A. Hansen, T. Vegge, Computational Screening of Doped α-MnO2 Catalysts for the Oxygen Evolution Reaction, ChemSusChem 11 (3) (2018) 629–637.
[13] C.W. Woon, H.R. Ong, K.F. Chong, K.M. Chan, M.M.R. Khan, MnO2/CNT as ORR electrocatalyst in air-cathode microbial fuel cells, Procedia Chem. 16 (2015) 640–647.
[14] Liew, K. B.; Daud, W. R. W.; Ghasemi, M.; Loh, K. S.; Ismail, M.; Lim, S. S.; Leong, J. X., Manganese oxide/functionalised carbon nanotubes nanocomposite as catalyst for oxygen reduction reaction in microbial fuel cell. international journal of hydrogen energy 2015, 40 (35), 11625-11632
[15] A. Serov, N.I. Andersen, A.J. Roy, I. Matanovic, K. Artyushkova, P. Atanassov, CuCo2O4 ORR/OER bi-functional catalyst: influence of synthetic approach on performance, J. Electrochem. Soc. 162 (4) (2015) F449.
[16] H. Osgood, S.V. Devaguptapu, H. Xu, J. Cho, G. Wu, Transition metal (Fe Co, Ni, and Mn) oxides for oxygen reduction and evolution bifunctional catalysts in alkaline media, Nano Today 11 (5) (2016) 601–625.
[17] Y. Chen, S. Ji, C. Chen, Q. Peng, D. Wang, Y. Li, Single-atom catalysts: synthetic strategies and electrochemical applications, Joule 2 (7) (2018) 1242–1264.
[18] C. Zhu, S. Fu, Q. Shi, D. Du, Y. Lin, Single-Atom Electrocatalysts, Angew. Chem. Int. Ed. (2017).
[19] A. Wang, J. Li, T. Zhang, Heterogeneous single-atom catalysis, Nat. Rev. Chem. 2 (6) (2018) 65–81.
[20] W. Liu, R. Yin, X. Xu, L. Zhang, W. Shi, X. Cao, Structural Engineering of Low-Dimensional Metal-Organic Frameworks: Synthesis, Properties, and Applications, Adv. Sci. 6 (12) (2019) 1802373.
[21] R.J. Kuppler, D.J. Timmons, Q.-R. Fang, J.-R. Li, T.A. Makal, M.D. Young, D. Yuan, D. Zhao, W. Zhuang, H.-C. Zhou, Potential applications of metal-organic frameworks, Coord. Chem. Rev. 253 (23–24) (2009) 3042–3066.
[22] G. Zhan, H.C. Zeng, Synthesis and Functionalization of Oriented Metal–Organic-Framework Nanosheets: Toward a Series of 2D Catalysts, Adv. Funct. Mater. 26 (19) (2016) 3268–3281.
[23] A.B. Sorokin, Phthalocyanine metal complexes in catalysis, Chem. Rev. 113 (10) (2013) 8152–8191.
[24] M. Abel, S. Clair, O. Ourdjini, M. Mossoyan, L. Porte, Single layer of polymeric Fe-phthalocyanine: an organometallic sheet on metal and thin insulating film, J. Am. Chem. Soc. 133 (5) (2010) 1203–1205.
[25] Y. Li, Q. Sun, The superior catalytic CO oxidation capacity of a Cr-phthalocyanine porous sheet, Sci. Rep. 4 (2014).
[26] Y. Wang, H. Yuan, Y. Li, Z. Chen, Two-dimensional iron-phthalocyanine (Fe-Pc) monolayer as a promising single-atom-catalyst for oxygen reduction reaction: a computational study, Nanoscale 7 (27) (2015) 11633–11641.
[27] Q. Deng, J. Pan, X. Yin, X. Wang, L. Zhao, S.-G. Kang, C.A. Jimenez-Cruz, R. Zhou, J. Li, Toward high permeability, selectivity and controllability of water desalination with FePc nanopores, PCCP 18 (11) (2016) 8140–8147.
[28] Q. Deng, L. Zhao, X. Gao, M. Zhang, Y. Luo, Y. Zhao, Single Layer of Polymeric Cobalt Phthalocyanine: Promising Low-Cost and High-Activity Nanocatalysts for CO Oxidation, Small 9 (20) (2013) 3506–3513.
[29] Haynes, W.; Lide, D., CRC handbook of chemistry and physics: a ready-reference book of chemical and physical data. 2011. Boca Raton, FL.: CRC Press: 2011.
[30] H.A. Hansen, J. Rossmeisl, J.K. Nørskov, Surface Pourbaix diagrams and oxygen reduction activity of Pt, Ag and Ni (111) surfaces studied by DFT, PCCP 10 (25) (2008) 3722–3730.
[31] J. Greeley, I. Stephens, A. Bondarenko, T.P. Johansson, H.A. Hansen, T. Jaramillo, J. Rossmeisl, I. Chorkendorff, J.K. Nørskov, Alloys of platinum and early transition metals as oxygen reduction electrocatalysts, Nat. Chem. 1 (7) (2009) 552.
[32] G. Gao, E.R. Waclawik, A. Du, Computational screening of two-dimensional coordination polymers as efficient catalysts for oxygen evolution and reduction reaction, J. Catal. 352 (2017) 579–585.
[33] N. Lahiri, N. Lotfizadeh, R. Tsuchikawa, V.V. Deshpande, J. Louie, Hexaaminobenzene as a building block for a Family of 2D Coordination Polymers, J. Am. Chem. Soc. 139 (1) (2016) 19–22.
[34] A. Nafady, A.P. O'Mullane, A.M. Bond, Electrochemical and photochemical routes to semiconducting transition metal-tetracyanoquinodimethane coordination polymers, Coord. Chem. Rev. 268 (2014) 101–142.

[35] X. Zhang, M.R. Saber, A.P. Prosvirin, J.H. Reibenspies, L. Sun, M. Ballesteros-Rivas, H. Zhao, K.R. Dunbar, Magnetic ordering in TCNQ-based metal–organic frameworks with host–guest interactions, Inorg. Chem. Front. 2 (10) (2015) 904–911.
[36] Y. Ma, Y. Dai, W. Wei, L. Yu, B. Huang, Novel Two-Dimensional Tetragonal Monolayer: Metal–TCNQ Networks, J. Phys. Chem. A 117 (24) (2013) 5171–5177.
[37] G. Zhu, Q. Sun, Recent advances in computational studies of organometallic sheets: magnetism, adsorption and catalysis, Comput. Mater. Sci. 112 (2016) 492–502.
[38] N. Wang, L. Feng, Y. Shang, J. Zhao, Q. Cai, P. Jin, Two-dimensional iron–tetracyanoquinodimethane (Fe–TCNQ) monolayer: an efficient electrocatalyst for the oxygen reduction reaction, RSC Adv. 6 (77) (2016) 72952–72958.
[39] C.A. Downes, S.C. Marinescu, One dimensional metal dithiolene (M= Ni, Fe, Zn) coordination polymers for the hydrogen evolution reaction, Dalton Trans. 45 (48) (2016) 19311–19321.
[40] C.A. Downes, S.C. Marinescu, Efficient electrochemical and photoelectrochemical H2 production from water by a cobalt dithiolene one-dimensional metal–organic surface, J. Am. Chem. Soc. 137 (43) (2015) 13740–13743.
[41] J.P. Perdew, K. Burke, M. Ernzerhof, Generalized gradient approximation made simple, Phys. Rev. Lett. 77 (18) (1996) 3865–3868.
[42] G. Kresse, J. Furthmüller, Efficient iterative schemes for ab initio total-energy calculations using a plane-wave basis set, Physical review B 54 (16) (1996) 11169.
[43] J. Wellendorff, K.T. Lundgaard, A. Møgelhøj, V. Petzold, D.D. Landis, J.K. Nørskov, T. Bligaard, K.W. Jacobsen, Density functionals for surface science: Exchange-correlation model development with Bayesian error estimation, Physical Review B 85 (23) (2012) 235149.
[44] K. Mathew, R. Sundararaman, K. Letchworth-Weaver, T. Arias, R.G. Hennig, Implicit solvation model for density-functional study of nanocrystal surfaces and reaction pathways, J. Chem. Phys. 140 (8) (2014) 084106.
[45] H.J. Monkhorst, J.D. Pack, Special points for Brillouin-zone integrations, Phys. Rev. B 13 (12) (1976) 5188.
[46] A. Larsen, J. Mortensen, J. Blomqvist, I. Castelli, R. Christensen, M. Dulak, J. Friis, M. Groves, B. Hammer, C. Hargus, The Atomic Simulation Environment—A Python library for working with atoms, J. Phys. Condens. Matter. (2017).
[47] V. Tripković, E. Skúlason, S. Siahrostami, J.K. Nørskov, J. Rossmeisl, The oxygen reduction reaction mechanism on Pt (1 1 1) from density functional theory calculations, Electrochim. Acta 55 (27) (2010) 7975–7981.
[48] Q. Deng, T. Wu, G. Chen, H.A. Hansen, T. Vegge, Combinatorial selection of a two-dimensional 3d-TM-tetracyanoquinodimethane (TM-TCNQ) monolayer as a high-activity nanocatalyst for CO oxidation, PCCP 20 (7) (2018) 5173–5179.
[49] Q. Deng, J. Zhao, T. Wu, G. Chen, H.A. Hansen, T. Vegge, 2D transition metal–TCNQ sheets as bifunctional single-atom catalysts for oxygen reduction and evolution reaction (ORR/OER), J. Catal. 370 (2019) 378–384.
[50] I.C. Man, H.Y. Su, F. Calle-Vallejo, H.A. Hansen, J.I. Martínez, N.G. Inoglu, J. Kitchin, T.F. Jaramillo, J.K. Nørskov, J. Rossmeisl, Universality in oxygen evolution electrocatalysis on oxide surfaces, ChemCatChem 3 (7) (2011) 1159–1165.
[51] J. Rossmeisl, A. Logadottir, J.K. Nørskov, Electrolysis of water on (oxidized) metal surfaces, Chem. Phys. 319 (1) (2005) 178–184.
[52] S. Divanis, T. Kutlusoy, I.M.I. Boye, I.C. Man, J. Rossmeisl, Oxygen evolution reaction: a perspective on a decade of atomic scale simulations, Chem. Sci. 11 (11) (2020) 2943–2950.
[53] F. Calle-Vallejo, A. Krabbe, J.M. García-Lastra, How covalence breaks adsorption-energy scaling relations and solvation restores them, Chem. Sci. 8 (1) (2017) 124–130.
[54] Q. Deng, T. Wu, G. Chen, H.A. Hansen, T. Vegge, Combinatorial Selection of Two-dimensional 3d-TM–tetracyanoquinodimethane (TM–TCNQ) Monolayer as High-Activity Nanocatalysts for CO Oxidation, PCCP (2018).
[55] J.K. Nørskov, J. Rossmeisl, A. Logadottir, L. Lindqvist, J.R. Kitchin, T. Bligaard, H. Jonsson, Origin of the overpotential for oxygen reduction at a fuel-cell cathode, J. Phys. Chem. B 108 (46) (2004) 17886–17892.
[56] M. Reda, H.A. Hansen, T. Vegge, DFT Study of the oxygen reduction reaction on carbon-coated iron and iron carbide, ACS Catal. 8 (11) (2018) 10521–10529.
[57] S. Cahangirov, H. Sahin, G. Le Lay, A. Rubio, Strain engineering of 2D materials, in: Introduction to the Physics of Silicene and other 2D Materials, Springer, 2017, pp. 87–96.
[58] R. Roldán, A. Castellanos-Gomez, E. Cappelluti, F. Guinea, Strain engineering in semiconducting two-dimensional crystals, J. Phys.: Condens. Matter 27 (31) (2015) 313201.
[59] M.A. Bissett, M. Tsuji, H. Ago, Strain engineering the properties of graphene and other two-dimensional crystals, PCCP 16 (23) (2014) 11124–11138.
[60] Scalise, E.; Houssa, M.; Pourtois, G.; Afanas'ev, V.; Stesmans, A., Strain-induced semiconductor to metal transition in the two-dimensional honeycomb structure of MoS 2. Nano Research 2012, 5 (1), 43-48.
[61] S. Kaniber, L. Song, J. Kotthaus, A. Holleitner, Photocurrent properties of freely suspended carbon nanotubes under uniaxial strain, Appl. Phys. Lett. 94 (26) (2009) 261106.
[62] L. Kou, A. Du, C. Chen, T. Frauenheim, Strain engineering of selective chemical adsorption on monolayer MoS 2, Nanoscale 6 (10) (2014) 5156–5161.
[63] K.L. Svane, M. Reda, T. Vegge, H.A. Hansen, Improving the Activity of M− N4 Catalysts for the Oxygen Reduction Reaction by Electrolyte Adsorption, ChemSusChem 12 (23) (2019) 5133–5141.
[64] V. Viswanathan, H.A. Hansen, Unifying Solution and Surface Electrochemistry: Limitations and opportunities in surface electrocatalysis, Top. Catal. 57 (1–4) (2014) 215–221.
[65] Q. Zhang, A. Asthagiri, Solvation effects on DFT predictions of ORR activity on metal surfaces, Catal. Today 323 (2019) 35–43.
[66] Y. Basdogan, A.M. Maldonado, J.A. Keith, Advances and challenges in modeling solvated reaction mechanisms for renewable fuels and chemicals, Wiley Interdisciplinary Rev. Comput. Mol. Sci. 10 (2) (2020) e1446.
[67] V. Tripkovic, Thermodynamic assessment of the oxygen reduction activity in aqueous solutions, PCCP 19 (43) (2017) 29381–29388.
[68] Rendón-Calle, A.; Builes, S.; Calle-Vallejo, F., Substantial improvement of electrocatalytic predictions by systematic assessment of solvent effects on adsorption energies. Applied Catalysis B: Environmental 2020, 119147
[69] A. Clayborne, H.J. Chun, R.B. Rankin, J. Greeley, Elucidation of pathways for NO electroreduction on Pt (111) from first principles, Angew. Chem. 127 (28) (2015) 8373–8376.
[70] M. Reda, H.A. Hansen, T. Vegge, DFT study of stabilization effects on N-doped graphene for ORR catalysis, Catal. Today 312 (2018) 118–125.
[71] C. Yang, G. Rousse, K.L. Svane, P.E. Pearce, A.M. Abakumov, M. Deschamps, G. Cibin, A.V. Chadwick, D.A. Dalla Corte, H.A. Hansen, Cation insertion to break the activity/stability relationship for highly active oxygen evolution reaction catalyst, Nat. Commun. 11 (1) (2020) 1–10.
[72] S. Back, A.R. Kulkarni, S. Siahrostami, Single Metal Atoms Anchored in Two-Dimensional Materials: Bifunctional Catalysts for Fuel Cell Applications, ChemCatChem 10 (14) (2018) 3034–3039.
[73] H.H. Heenen, J.A. Gauthier, H.H. Kristoffersen, T. Ludwig, K. Chan, Solvation at metal/water interfaces: An ab initio molecular dynamics benchmark of common computational approaches, J. Chem. Phys. 152 (14) (2020) 144703.
[74] T. Zhang, L. Zhu, G. Chen, Electron-doping induced half-metallicity in one-dimensional Co-dithiolene molecular wires, J. Mater. Chem. C 4 (43) (2016) 10209–10214.
[75] G. Giorgi, J.-I. Fujisawa, H. Segawa, K. Yamashita, Small photocarrier effective masses featuring ambipolar transport in methylammonium lead iodide perovskite: a density functional analysis, J. Phys. Chem. Lett. 4 (24) (2013) 4213–4216.
[76] J. Zhao, Q. Deng, A. Bachmatiuk, G. Sandeep, A. Popov, J. Eckert, M.H. Rummeli, Free-standing single-atom-thick iron membranes suspended in graphene pores, Science 343 (6176) (2014) 1228–1232.